Electronic Supplementary Information

Understanding the Raman enhancement of carbon nanohorns labelled with organic dyes

Daniel Iglesias,[#a,b] Raúl Martín,[#a,d] Miguel Ángel Álvarez,[a,b] Irene Badía-Domínguez,[c] Ester Vázquez,[a,b] M. Carmen Ruiz Delgado,*[c] Pilar Prieto,*[a] and M. Antonia Herrero.*[a,b]

a. Facultad de Ciencias y Tecnologías Químicas, Universidad de Castilla-La Mancha (UCLM), 13071 Ciudad Real, Spain.

b. Instituto Regional de investigación Científica Aplicada (IRICA), 13071 Ciudad Real, Spain.

c. Department of Physical Chemistry, University of Malaga, Campus de Teatinos s/n, Malaga 29071, Spain.

d. Instituto de Ciencia de Materiales de Madrid, CSIC Cantoblanco, 28049, Madrid,Spain

# These authors contributed equally to this work.

Table of Contents

1. General Information

1.1. Chemicals

All chemicals and solvents were purchased from commercial suppliers and used as-received. Single walled carbon nanohorns (CNHs) were purchased from Carbonium S.R.L.

1.2. Characterization techniques

Thermogravimetric Analysis (TGA) was carried out using a TGA Q50 TA Instruments. Samples were heated from 100 to 800 °C with a ramp of 10°C/min under N_2 atmosphere.

The **ultrasonication** was carried out on an ultrasonic bath Bandelin Sonorex Digitec operating with an ultrasound frequency of 35 kHz and a nominal ultrasonic power of 215 W.

Microwave irradiations were performed in a Discovers (CEM) focused microwave reactor.

Flash **chromatography** was performed using silica gel (Merck, Kieselgel 60, 230–240 mesh or Scharlau 60, 230–240 mesh) or CombiFlash Rf+ Teledyne Isco equipment.

Nuclear magnetic resonance (NMR) spectra were recorded using a Varian Unity Inova 500 (^{1}H: 500 MHz; ^{13}C: 125 MHz) spectrometer at 298 K using deuterated solvents and are internally referenced against the residual portion of solvent signal. Coupling constants (*J*) are denoted in Hz and chemical shifts (δ) in ppm. Multiplicities are denoted as follows: s = singlet, d = doublet, t = triplet, q = quartet, and m = multiplet. NMR data were processed using the MestReNova 10.0.2 software package.

MALDI-TOF mass spectra were recorded using a Bruker Autoflex II TOF/TOF spectrometer with 2,5-dihydroxybenzoic acid (DHB) as the matrix. Samples co-crystallized with the matrix on the probe were ionized using a nitrogen laser pulse (337 nm) and accelerated under 20 kV with time-delayed extraction before entering the time-of-flight mass spectrometer. The matrix (10 mg ml^{-1}) and sample (1 mg ml^{-1}) were dissolved separately in chloroform and mixed in a matrix/sample ratio ranging from 100:1 to 50:1. MALDITOF MS in positive reflector mode was used for all samples.

The **melting points** were determined using a Buchi Meltingpoint 565 apparatus.

UV-Vis spectroscopy was performed using a Varian Cary 5000 spectrophotometer using 1 cm pathlength quartz cuvettes.

Fluorescence spectroscopy was performed using a Cary 5000 UV-Vis-NIR spectrophotometer. The quenching of **TDQ-1** and **TDQ-2** in the presence of CNHs was determined at low CNH concentrations (below 0.05 mg/L). The concentration of the corresponding TDQ was kept constant in all measurements.

Raman spectra of the hybrids were recorded using an InVia Renishaw microspectrometer equipped with 532, 633 and 785 nm point-based lasers. A quantity of hybrids was first filtered through a Millipore membrane to generate a continuous film. This sample was then dried under vacuum and analyzed without further treatment. Two different types of measurements were performed. To study the effect of the laser and laser intensity, the samples were irradiated for 10 s at different laser power. To characterize the homogeneity and the effect of probe concentration, we used the Raman point-mapping method with the ×50 microscope and the 532 nm laser (max. power 9.77 mW). The samples were irradiated for 4 s (2 accumulations of 2 s each) while keeping the intensity at 0.1% of the maximum.

The FT-Raman spectra for **TDQ-1** and **TDQ-2** were recorded using an FT-Raman accessory kit (RamII)) linked to a Bruker Vertex70 spectrometer. A continuous-wave Nd-YAG laser working at λ=1064 nm was used for excitation, with a germanium detector operating at liquid nitrogen temperature. Raman scattering radiation was collected in a back-scattering geometry with a standard spectral resolution of 4 cm^{-1}. The power of the laser beam was kept at a level lower than 100 mW in all cases. Around 3000–4000 scans were averaged for each spectrum to optimize the signal-to-noise ratio.

Scanning electron microscopy images were collected under vacuum using a ZEISS GeminiSEM 500 field emission instrument (Zeiss, Germany) with an acceleration voltage of0.02−30 kV. This instrument is equipped with an energy dispersive X-ray analysis unit.

The **electrical sheet resistance** of the glass and paper substrates was measured using a four-point probe analyzer (RM3000, Jandel). The current was maintained between 0.1 and 0.5 μA. The electrical conductivities of the paper and glass substrates used in this work were below the limit of the instrument.

Density Functional Theory (DFT) calculations were carried out using the Gaussian 16 program.[1] The ωB97XD[2] functional with the standard 6-31G** basis set[3,4] was chosen given its accuracy when calculating dispersion forces such us hydrogen bonds and dipole-dipole interactions. All geometrical parameters were allowed to vary independently, and no symmetry constraints were imposed during the optimization process. For the calculation of the hybrids (CNH-TDQ systems), the adsorption energy was calculated as follows:

$$E_{ads} = E_{CNH-TDQ} - E_{CNH} - E_{TDQ} \qquad (eq.\,1)$$

where $E_{CNH\text{-}TDQ}$, E_{CNH}, and E_{TDQ} are the total energies of the total systems, the isolated CNH and the isolated thiadiazoloquinoxaline molecule, respectively.

The total adsorption energies were decomposed further into three main contributions:

$$E_{ads} = E_{interaction} + E_{CNH-dist} + E_{TDQ-dist} = \left(E_{CNH-TDQ} - E_{CNH'} - E_{TDQ'}\right) + \left(E_{CNH'} - E_{CNH}\right) + \left(E_{TDQ'} - E_{TDQ}\right) \qquad (eq.\,2)$$

where $E_{CNH'}$ and $E_{TDQ'}$ are the total energies of the carbon nanohorn and the TDQ derivatives in the aggregate, respectively, taken from the optimized CNH-TDQ system equilibrium structure.
This analysis gave the direct interaction energy between the **TDQ-1** and **TDQ-2** derivative and CNH ($E_{interaction}$), and the distortion energy of CNH ($E_{CNH\text{-}dist}$) and TDQ ($E_{TDQ\text{-}dist}$) from their unperturbed equilibrium structure. Table S3 shows these terms together with the total adsorption energy.

The calculated Raman frequencies were uniformly scaled by a factor of 0.945 to disentangle experimental misassignments. Then, theoretical Raman spectra were obtained by convolution of the scaled frequencies vs the Raman activities with Gaussian functions (4 cm^{-1} width at the half-height).

Furthermore, a time-dependent DFT (TD-DFT)[5,6] approach was used to assess the excited state vertical transition energies of the TDQ molecules. Absorption spectra were simulated through by convolution of these vertical transition energies and oscillator strengths with Gaussian functions characterized by a half width at half-maximum of 0.3 eV. Molecular orbital contours were plotted using GaussView 6.1.1.

2. Experimental protocols

2.1. Synthesis of TDQ-1 and TDQ-2

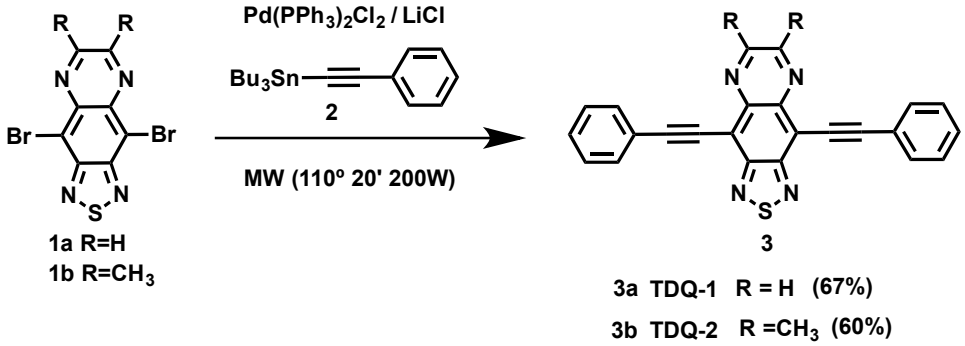

Scheme 1. General scheme of the synthesis of the derivatives TDQ-1 and TDQ-1

General procedure: A mixture of the quinoxaline derivative (**1**) (0.27 mmol), tributyl(phenylethynyl)tin (**2**) (0.274 g, 0.70 mmol), $Pd(PPh_3)_2Cl_2$ (0.008 g, 0.01 mmol) and LiCl (0.034 g, 0.08 mmol) was added to a dried microwave vessel under argon. The vessel was then closed and irradiated at 110 ºC for 20 min. The crude reaction product was purified by chromatography, eluting with hexane/ethyl acetate to afford analytically pure products **3 (TDQ-1 and TDQ-2)**.

Preparation of 4,9-bis(phenylethynyl)-[1,2,5]thiadiazolo[3,4-g]quinoxaline (TDQ-1). From derivative **1a** (0.093 g, 0.27 mmol), commercially available tributyl(phenylethynyl)tin (0.274 g, 0.70 mmol), derivative **TDQ-1** (0.070 g, 67%) was obtained as a purple solid by chromatography, eluting with hexane/ethyl acetate (3/1). M.p.: 210–211 ºC. ^{1}H-NMR ($CDCl_3$, ppm) δ: 9.02 (s, 2H, H-quinoxaline), 7.82 (d, J = 7.2 Hz, 4H, *o*-H), 7.45–7.42 (m, 6H, *m,p*-Harom).^{13}C-NMR ($CDCl_3$, ppm) δ: 154.1, 147.1, 142.1, 132.4, 129.5, 128.5, 122.7, 115.2, 106.5, 84.7. MS calcd for ($C_{24}H_{12}N_4S$) M+· 388.078, found 390.322.

Preparation of 6,7-dimethyl-4,9-bis(phenylethynyl)-[1,2,5]-thiadiazolo[3,4-g]quinoxaline (TDQ-2). From derivative **1b** (0.100 g, 0.27 mmol), commercially available tributyl(phenylethynyl)tin (0.312 g, 0.70 mmol), derivative **TDQ-2** (0.075 g, 60%) was obtained as a red solid by chromatography, eluting with hexane/ethyl acetate (3/1). M.p.: 220–222 ºC. ^{1}H-NMR ($CDCl_3$, ppm) δ: 7.83 (d, J = 7.3 Hz, 4H, *o*-H), 7.45–7.42 (m, 6H, *m, p*-H), 2.89 (s, 6H, -CH3). ^{13}C-NMR ($CDCl_3$, ppm) δ: 156.8, 152.7, 141.2, 132.3, 129.2, 128.4, 123.0, 113.6, 105.3, 84.8, 24.1. MS calcd for ($C_{26}H_{16}N_4S$) M+· 416.110, found 418.338.

2.2. Synthesis of CNH-1 and CNH-2.

The protocol is analogous for both derivatives.

The corresponding TDQ was dissolved in $CHCl_3$ to afford a 10^{-4} M solution. In a separate vial, 10 mg of pristine CNHs were dispersed in $CHCl_3$ (10 ml), and the sample was ultrasonicated for 10 min. The dispersion of CNHs (1 ml) was then added to the TDQ solution. The mixture was sonicated briefly (10 s) and stirred for 1 hour at room temperature in an orbital stirrer.

After that, the mixture was filtered through a Millipore membrane (JHWP04700, 0.45 μm) and washed with $CHCl_3$ to remove the unbound material, giving the hybrids as a black powder.

The same protocol was followed to assess the effect of probe concentration but changing the concentration of TDQ (*i.e.* 10^{-5} or 10^{-6} M).

3. Supplementary Figures

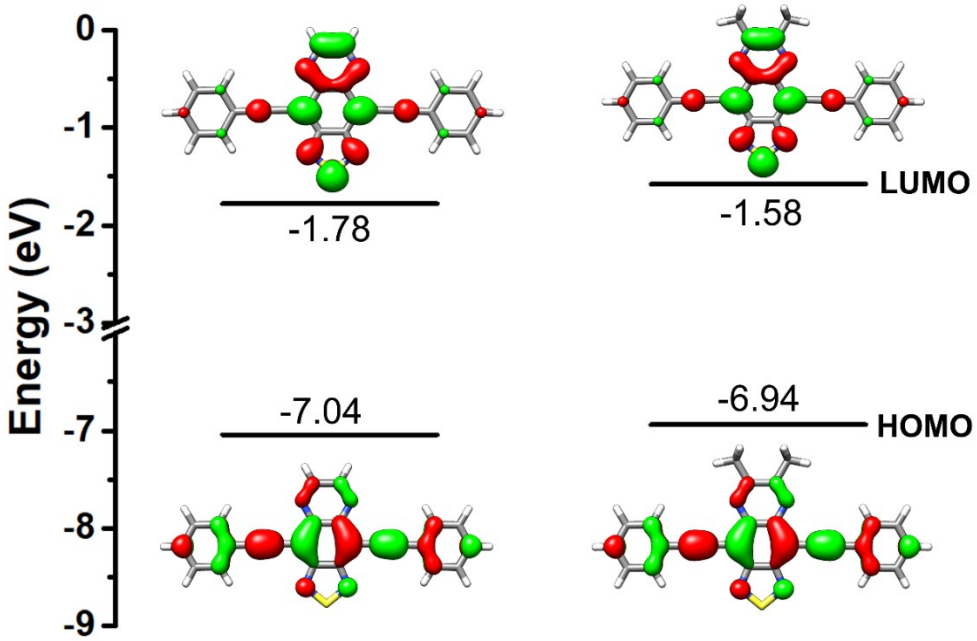

Figure S1. DFT-calculated HOMO and LUMO topologies for **TDQ-1** (a) and **TDQ-2** (b) systems at the ωB97XD/6-31G** level of theory.

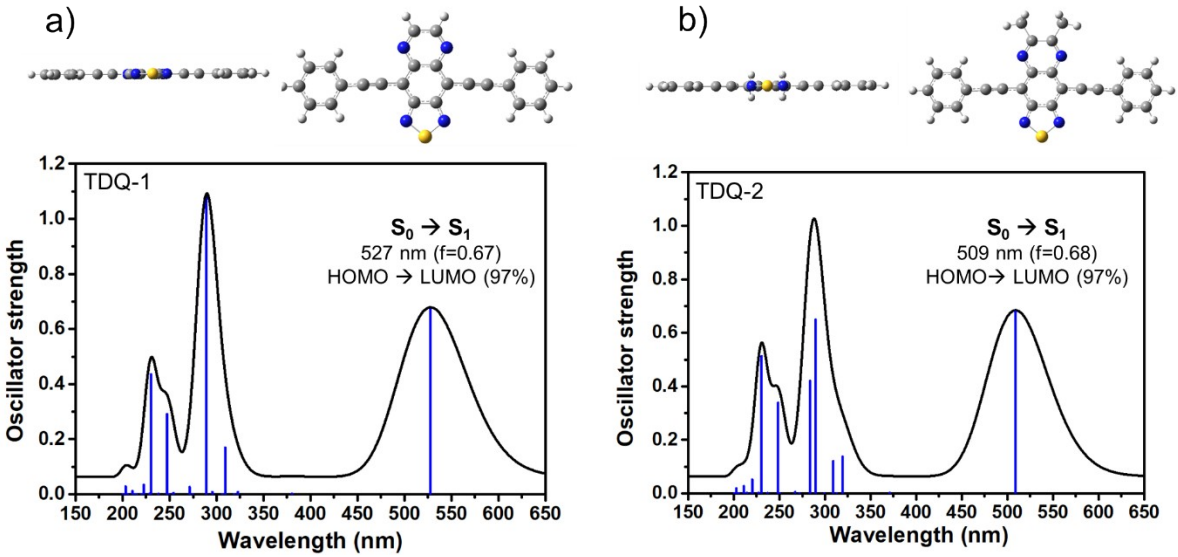

Figure S2. Top and lateral views of the DFT-optimized structures together with the TD-DFT-calculated vertical excited state transitions (blue solid bars) at the ωB97XD/6-31G** level for **TDQ-1** (a) and **TDQ-2** (b) systems.

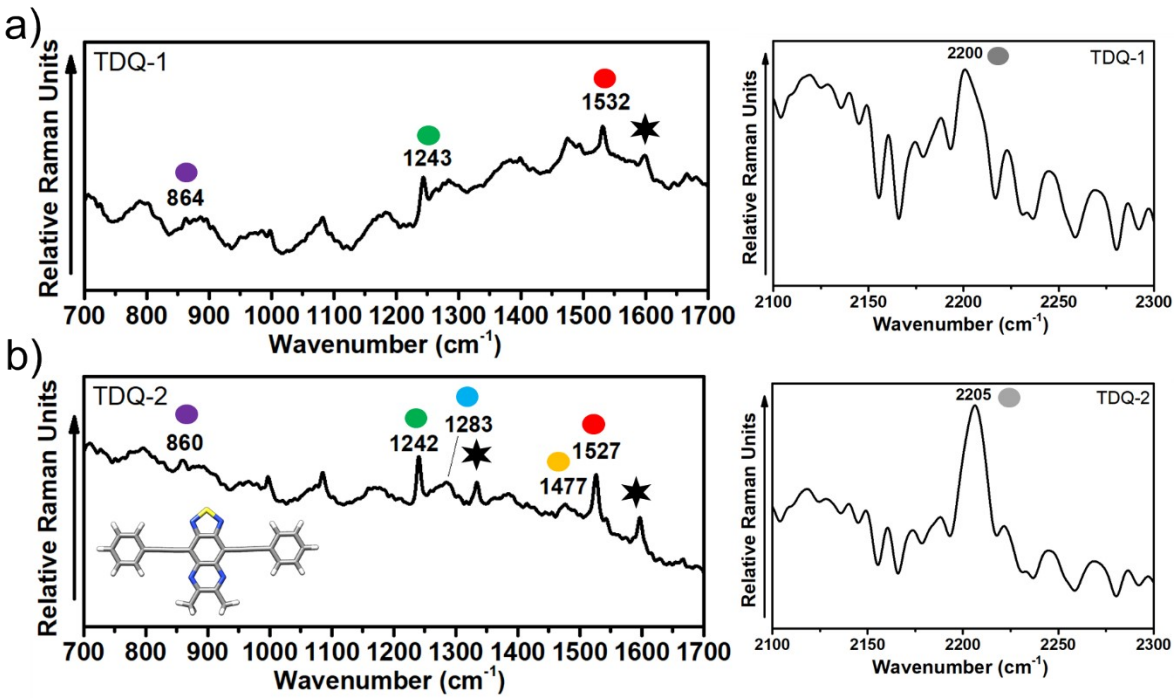

Figure S3. FT-Raman spectra of **TDQ-1** (a) and **TDQ-2** (b) as solid powders. The Raman bands denoted with black stars in **TDQ-1** and **TDQ-2** are hidden by the D and G-bands of the hybrid.

a)

Raman frequency (cm^{-1})	Description
2200 (2231)	C≡C stretching vibration of acetylene groups
1532 (1525)	CC and CN stretching vibration of quinoxilane unit
1243 (1233)	CH bending of pyrazine + CC stretching vibration of pyrazine
864 (845)	SN stretching vibration of thiadiazole

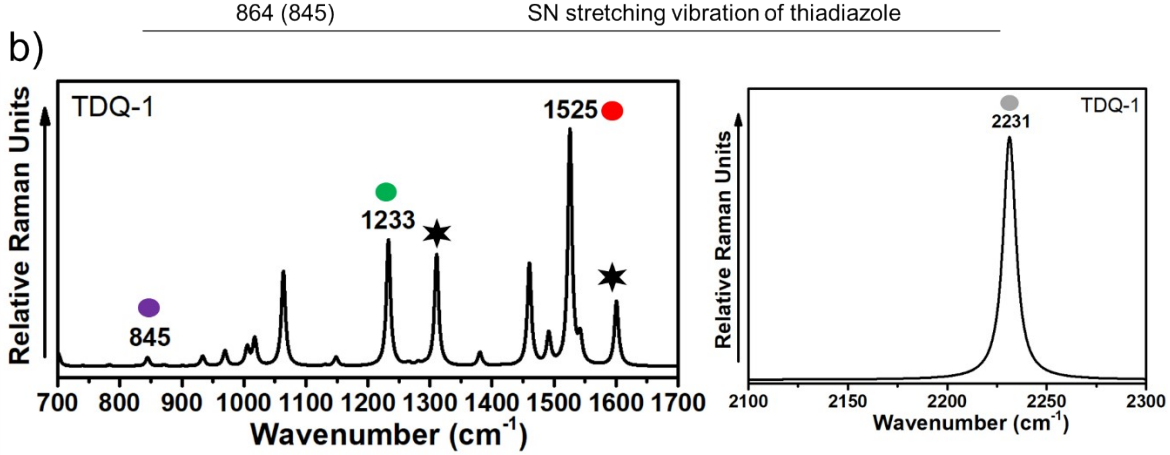

Figure S4. (a) Table with the description of the most relevant Raman bands (the theoretical Raman frequencies are in parentheses). (b) Theoretical Raman spectrum of **TDQ-1** at the ωB97XD/6-31G** level of theory. The Raman bands denoted with black stars in **TDQ-1** are hidden by the D and G-band of the hybrid.

a)

Raman frequency (cm^{-1})	Description
2205 (2234)	C≡C stretching vibration of acetylene groups
1527 (1525)	CC and CN stretching vibration of quinoxilane unit
1477 (1463)	CH bending of external phenyl rings + CC stretching of central TDQ unit
1283 (1266)	CH bending of external phenyl rings + CC stretching vibration of acetylene groups and central TDQ unit
1242 (1228)	CH bending of pyrazine + CC stretching vibration of pyrazine
860 (843)	SN stretching vibration of thiadiazole

b)

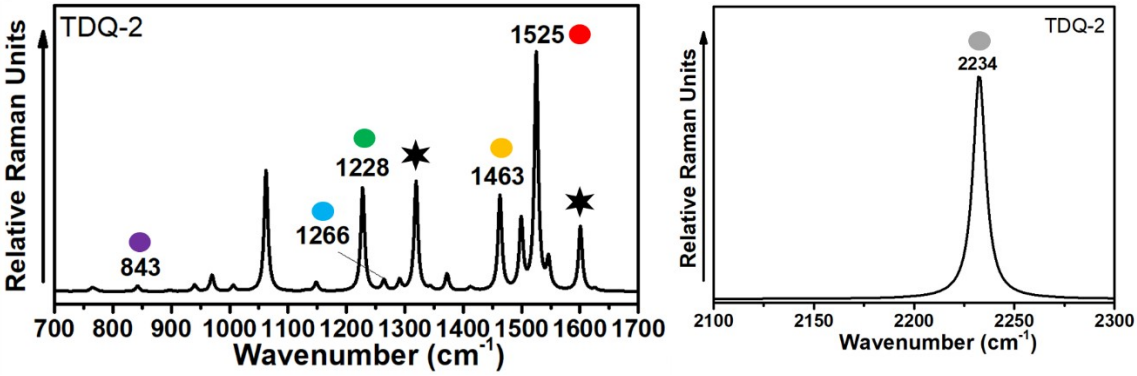

Figure S5. (a) Table with the description of the most relevant Raman bands (the theoretical Raman frequencies are in parentheses). (b) Theoretical Raman spectrum of **TDQ-2** at the ωB97XD/6-31G** level of theory. The Raman bands denoted with black stars in **TDQ-2** are hidden by the D and G-band of the hybrid.

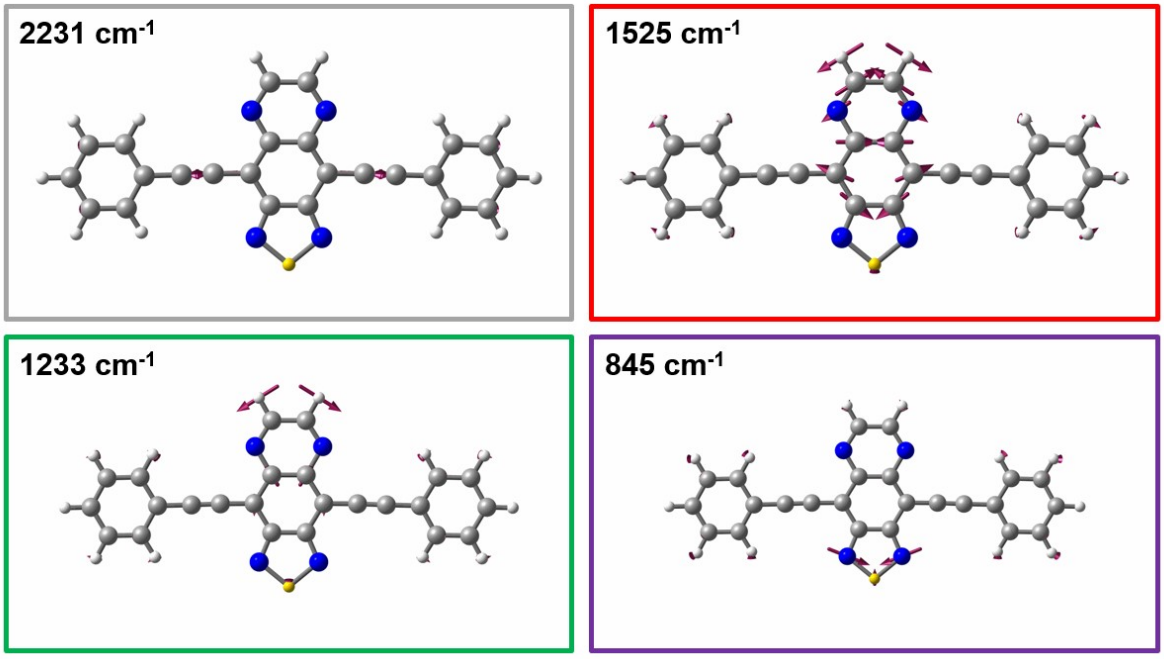

Figure S6. Schematic eigenvectors for the most relevant Raman modes of **TDQ-1**, computed at the ωB97XD/6-31G** level.

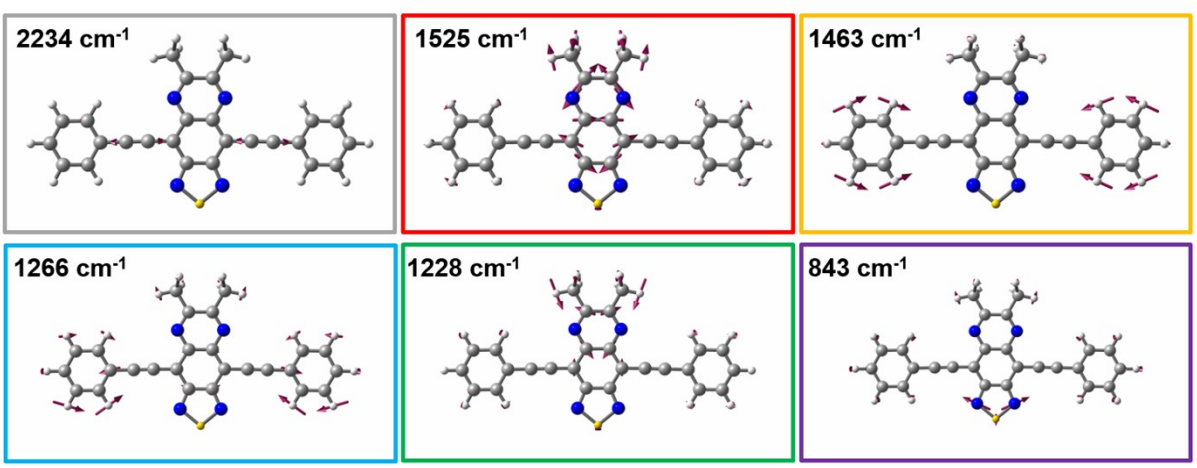

Figure S7. Schematic eigenvectors for the most relevant Raman modes of **TDQ-2**, computed at the ωB97XD/6-31G** level.

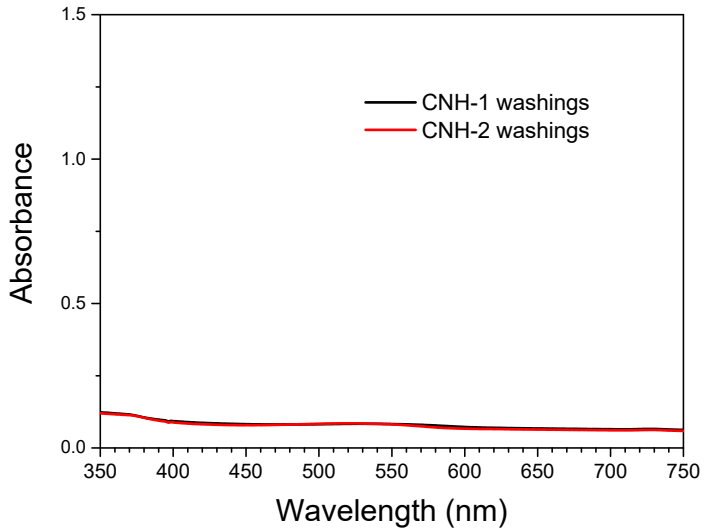

Figure S8. UV-Vis spectra of the washings showing that the amount of dye is negligible in both cases.

Figure S9. Dispersion of pristine CNHs (1 mg/ml, $CHCl_3$) four weeks after preparation. This illustrates the stability of the sample.

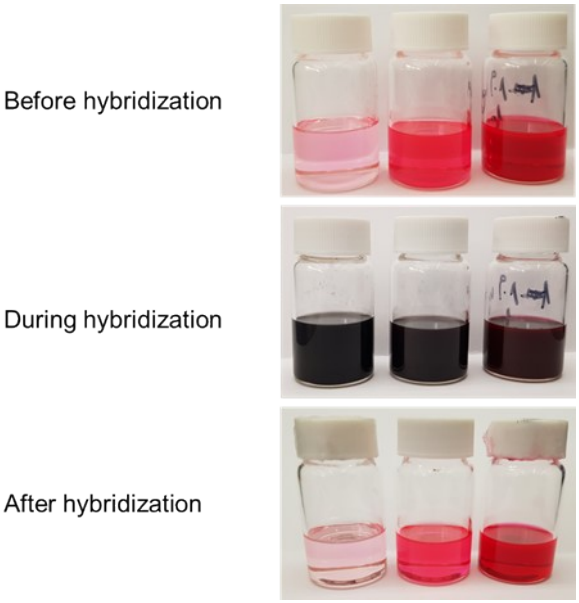

Figure S10. Pictures of **TDQ-2** solutions during the hybridization process showing that the unbound dye is fully recovered after the process. Left 10^{-6} M, center 10^{-5} M, and right 10^{-4} M.

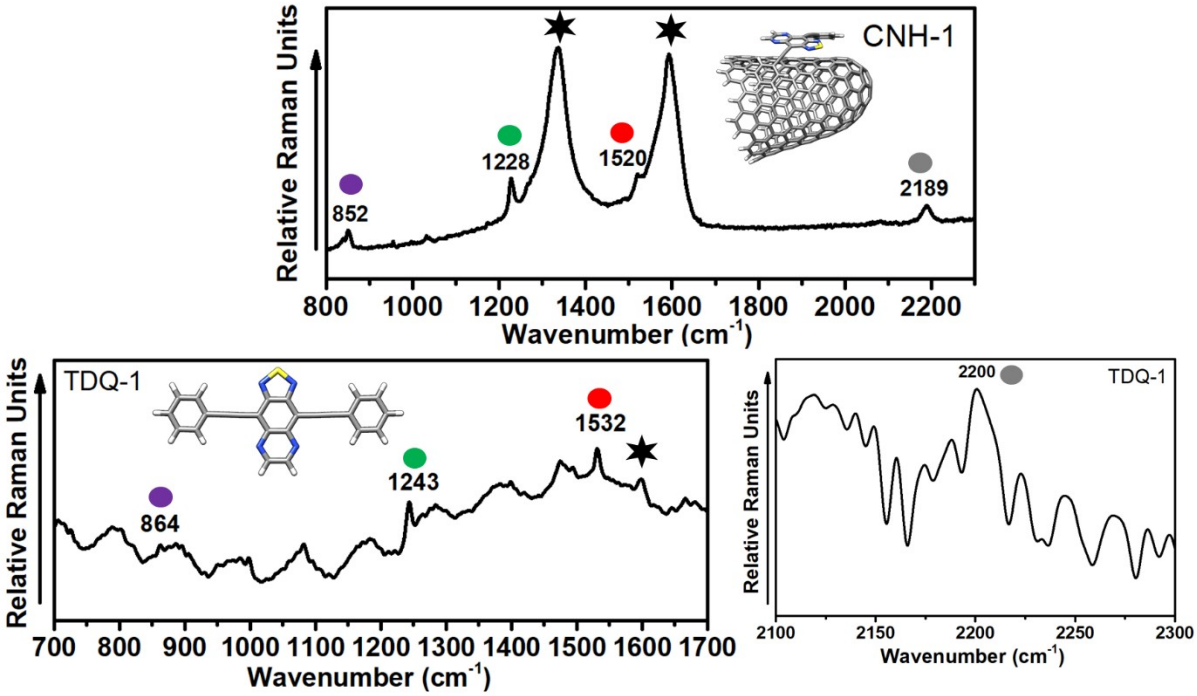

Figure S11. Comparison between the Raman spectrum of **CNH-1** (top) and the FT-Raman spectrum of **TDQ-1** (bottom). The Raman bands denoted with black stars in the organic sample **TDQ-1** are hidden by the G-band of the hybrid.

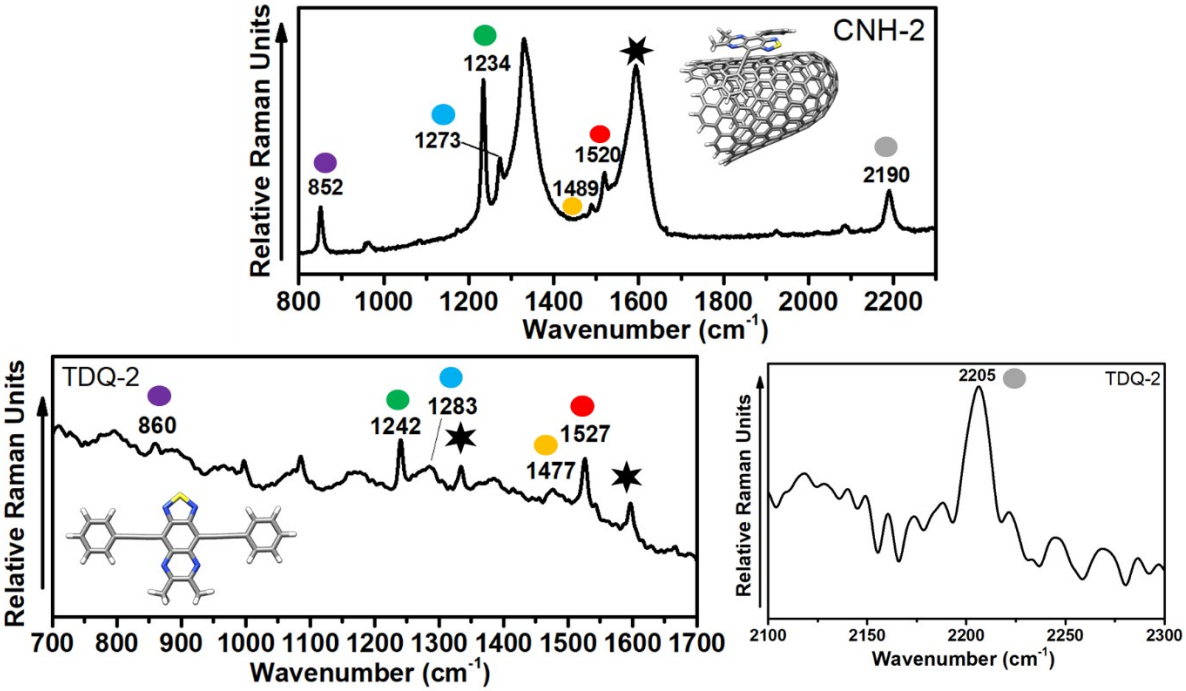

Figure S12. Comparison between the Raman spectrum of **CNH-2** (top) and the FT-Raman spectrum of **TDQ-2** (bottom). The Raman bands denoted with black stars in the organic sample **TDQ-2** are hidden by the D and G-band of the hybrid.

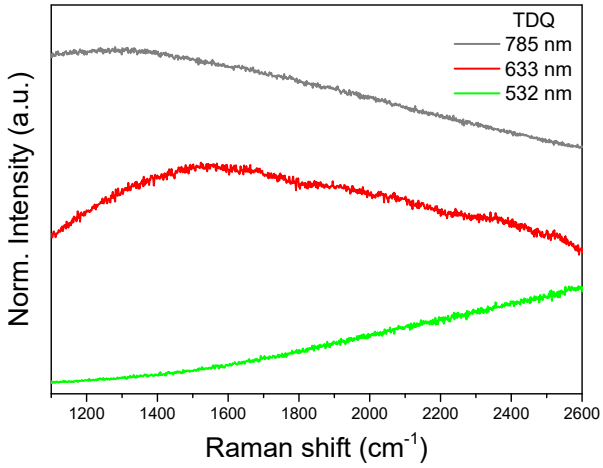

Figure S13. Representative Raman spectra of the dyes with the lasers used to characterize the hybrids.

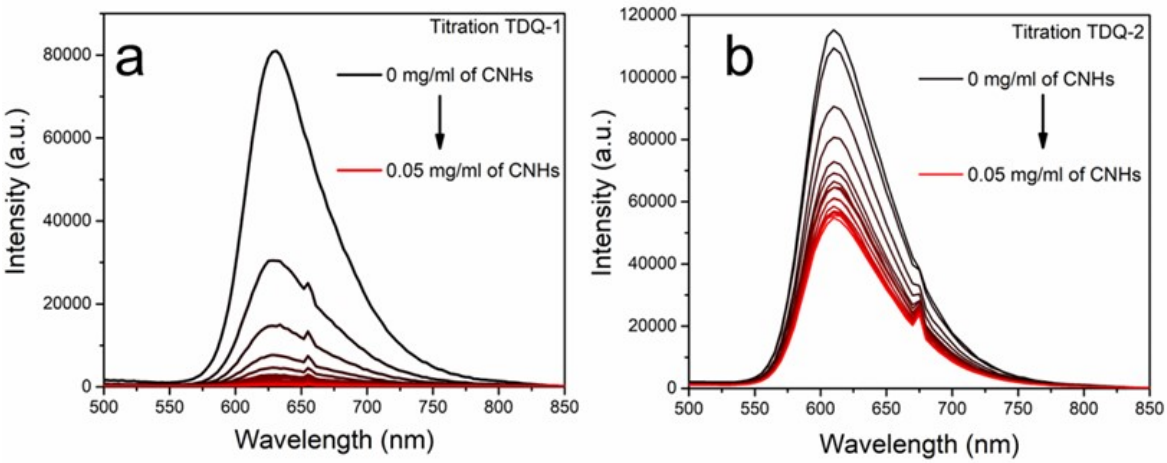

Figure S14. Fluorescence spectra of **TDQ-1** (a) and **TDQ-2** (b) upon addition of pristine CNHs. The concentration the corresponding TDQ is constant throughout the experiment.

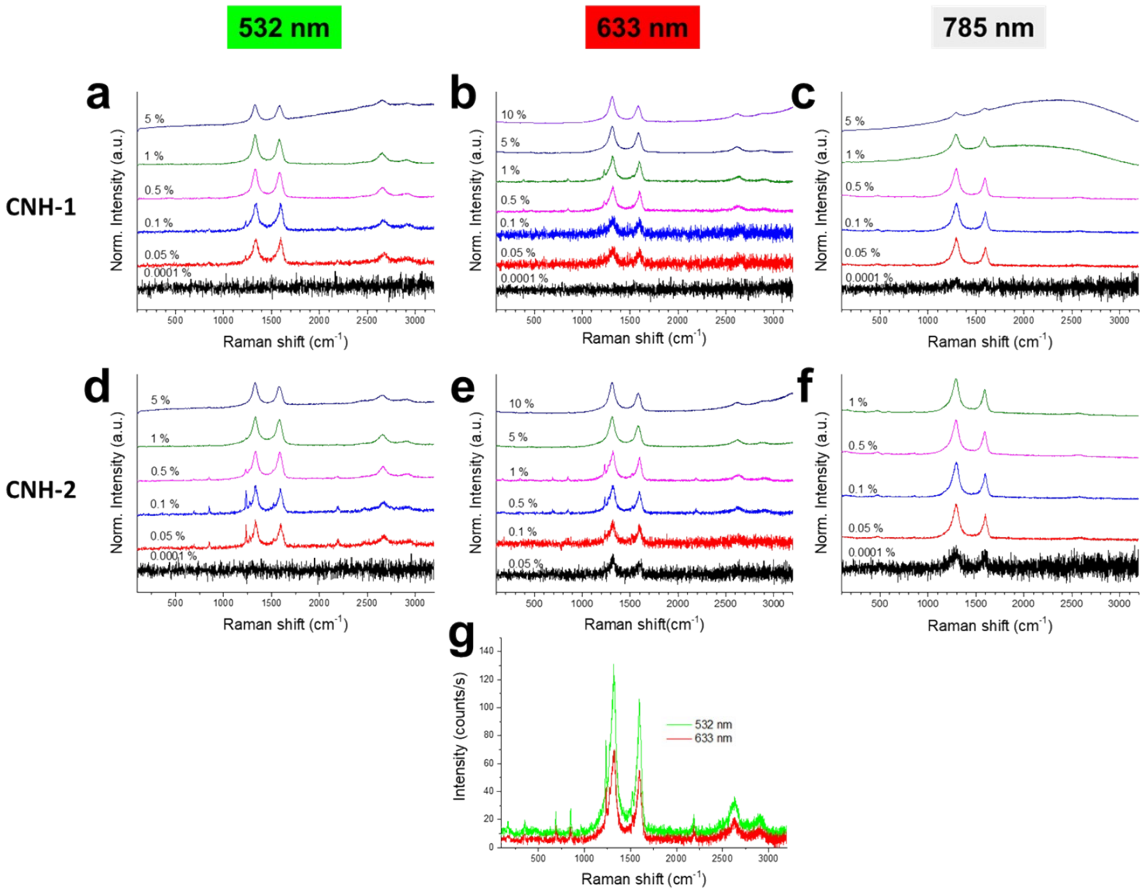

Figure S15. (a-f) Raman spectra of **CNH-1** and **CNH-2** acquired after irradiation at 532 nm, 633 nm and 785 nm, respectively, acquired at several power intensities. (g) Absolute intensities of the best conditions achieved with the green and red lasers showing the better performance for the most energetic light source for **CNH-2**.

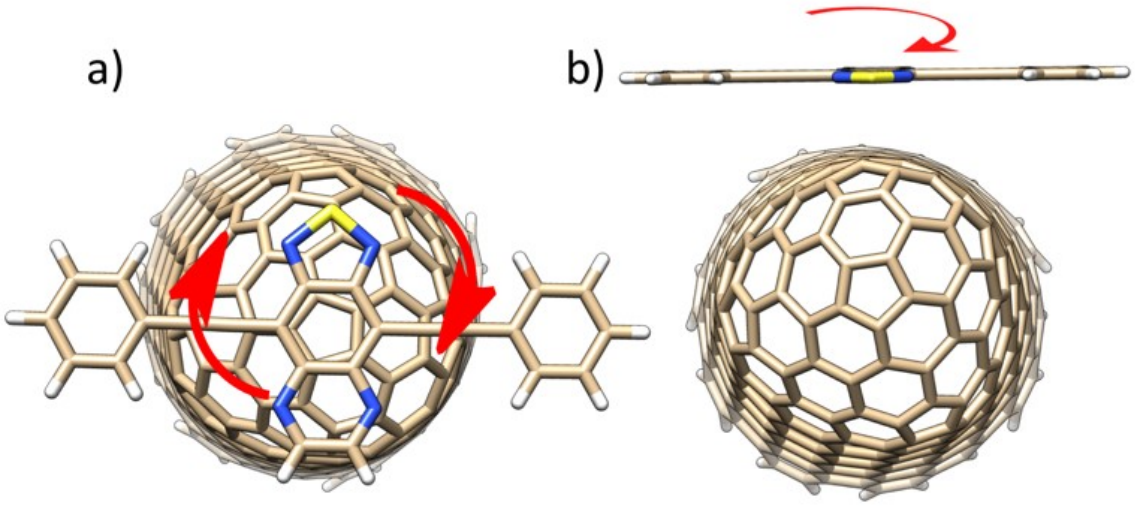

Figure S16. Adsorption of **TDQ-1** derivative on a) cone tip and b) lateral face of CNH. The red arrows represent the rotation of the molecule with respect to the nanohorn giving rise to the different CNH-TDQ dispositions displayed in Figures S17-S18.

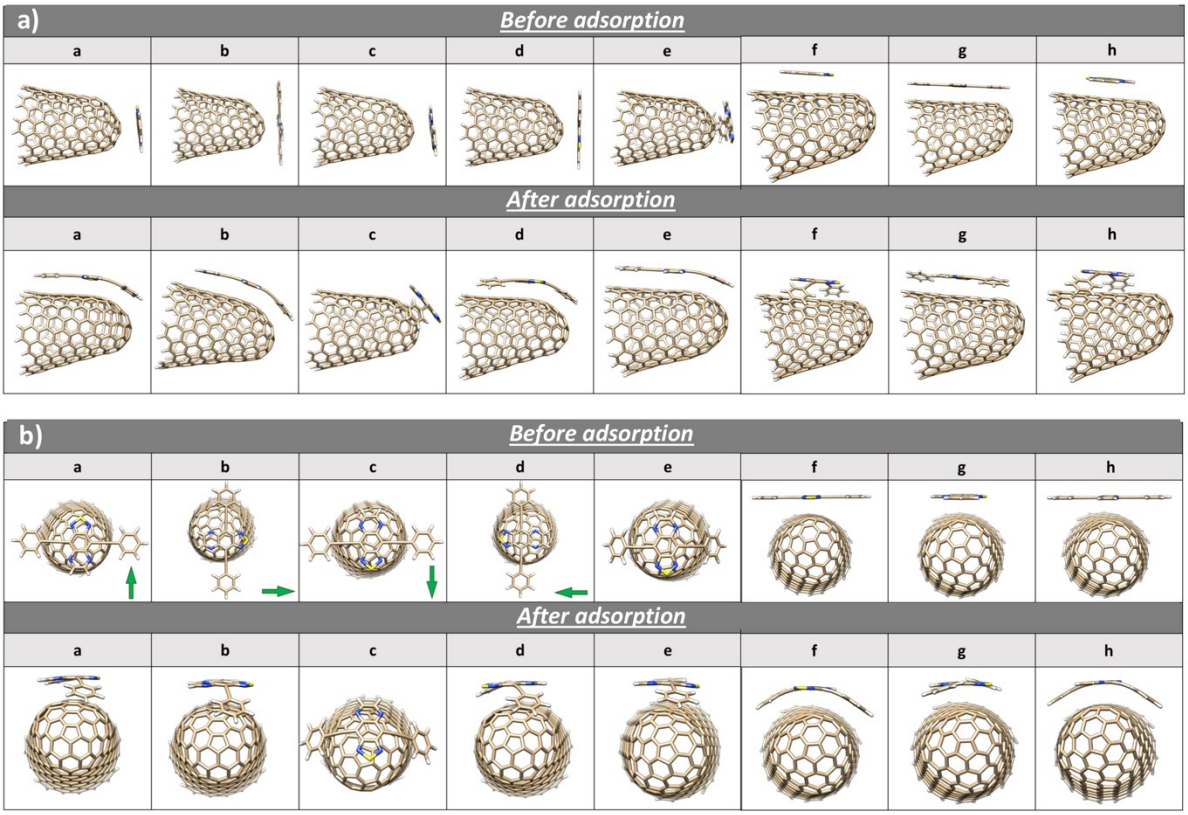

Figure S17. Initial and optimized structures of CNH and **TDQ-1 (CNH-1)** for the different dispositions calculated at the ωB97XD/6-31G** level a) Front view, b) Top view. The tip of the green arrow indicates the sulfur atom position in the molecule.

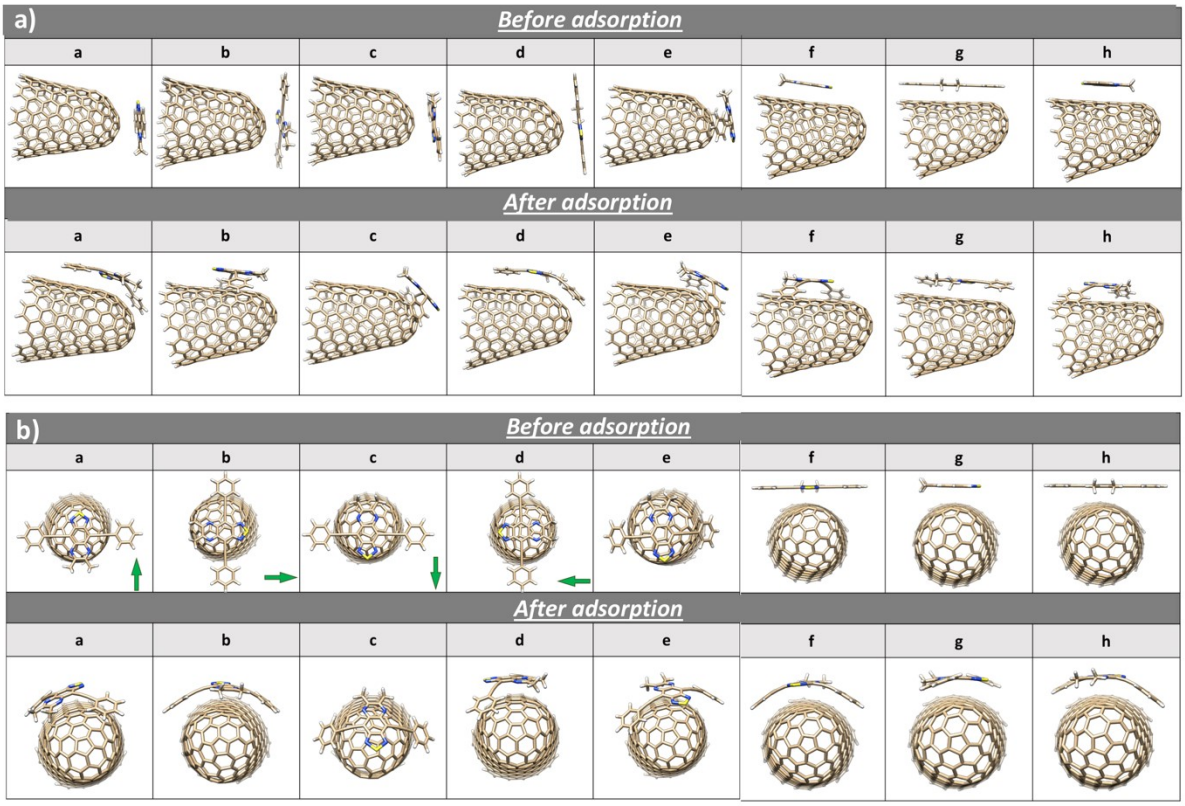

Figure S18. Initial and optimized structures of CNH and **TDQ-2** (**CNH-2**) for the different dispositions calculated at the ωB97XD /6-31G** level a) Front view, b) Top view. The tip of the green arrow indicates the sulfur atom position in the molecule.

Table S1. Adsorption energy decomposition for the studied orientations of **TDQ-1** and **TDQ-2** derivatives adsorbed on CNH calculated at the ωB97XD /6-31G** level. Energy values are giving in eV.

Disposition	CNH-1				CNH-2			
	E_{ads}	E_{ads} decomposition			E_{ads}	E_{ads} decomposition		
		$E_{interaction}$	$E_{TDQ'}$	$E_{CNH'}$		$E_{interaction}$	$E_{TDQ'}$	$E_{CNH'}$
a	-1.66	-1.76	0.11	0.00	-1.68	-1.87	0.20	0.00
b	-1.63	-1.74	0.12	-0.01	-1.85	-2.10	0.24	0.01
c	-1.13	-1.47	0.33	0.01	-1.27	-1.61	0.33	0.01
d	-1.70	-1.80	0.12	-0.02	-1.73	-1.88	0.16	-0.01
e	-1.69	-1.76	0.08	-0.01	-1.37	-1.66	0.29	0.00
f	-1.80	-1.97	0.17	0.00	-1.93	-2.15	0.22	0.00
g	-1.82	-1.87	0.04	0.01	-1.94	-2.02	0.07	0.01
h	-1.88	-2.04	0.17	-0.01	-2.09	-2.26	0.16	0.00

Table S2. Bending angles of **TDQ-1** and **TDQ-2** derivatives when adsorbed on CNH in the different dispositions (a-h).

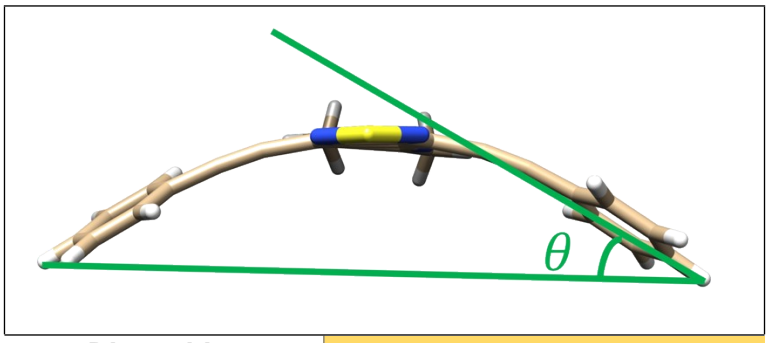

Disposition	CNH-1 (θ)	CNH-2 (θ)
a	12.0	21.3
b	15.9	27.5
c	18.0	20.3
d	31.3	31.0
e	6.8	28.5
f	21.5	25.5
g	4.8	6.7
h	21.0	20.2

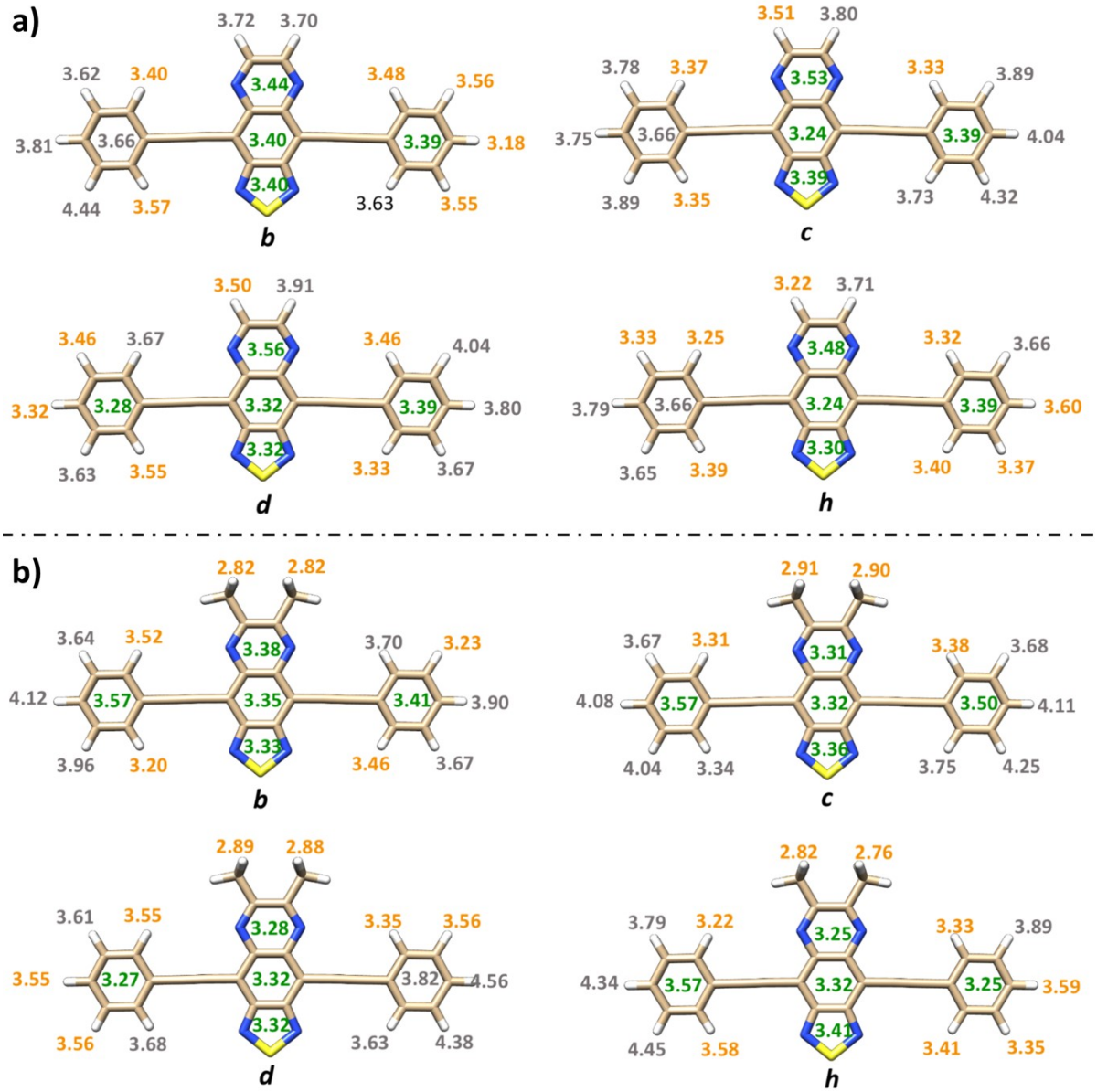

Figure S19. CH-π (orange numbers) and π-π distances (green numbers) for a) **CNH-1** and b) **CNH-2** in *b*, *c*, *d* and *h* dispositions. All distances are indicated in Angstroms (Å). Distances greater than 3.60 Å are shown in grey. CH-π distances were measured between the corresponding TDQ hydrogen and the shortest neighboring carbon atom of the nanohorn while π-π distances were measured between the shortest neighboring carbon atoms of the nanohorn and the TDQ.

Table S3. Number of CH-π and π-π interactions between **TDQ-1** and **TDQ-2** derivatives and CNH for the different dispositions.

Disposition	CNH-1		CNH-2	
	CH-π / π-π interactions < 3.30 Å	**CH-π / π-π interactions [3.30-3.60] Å**	**CH-π / π-π interactions < 3.30 Å**	**CH-π / π-π interactions [3.30-3.60] Å**
b	1 / 0	5 / 4	4 / 0	2 / 5
c	0 / 1	4 / 3	2 / 0	2 / 5
d	0 / 1	6 / 4	2 / 2	5 / 2

h	2 / 1	6 / 3	3 / 2	5 / 3

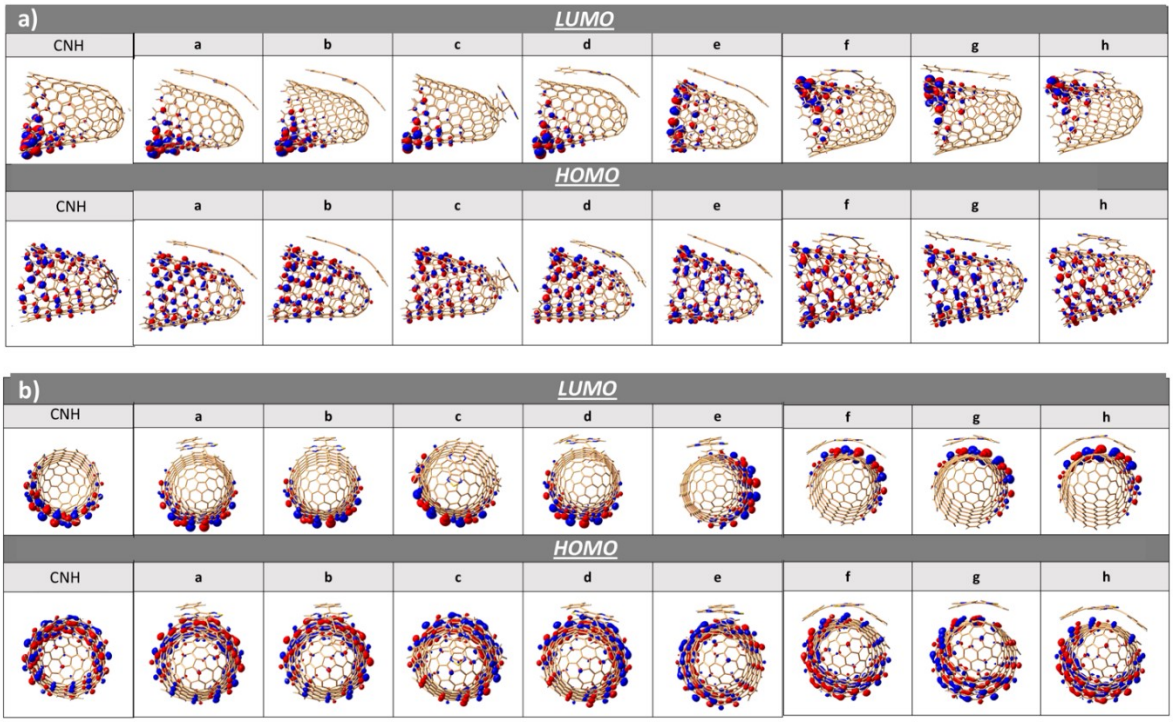

Figure S20 HOMO and LUMO orbitals for **CNH-1** in the different dispositions calculated at the ωB97XD /6-31G** level a) Front view, b) Top view.

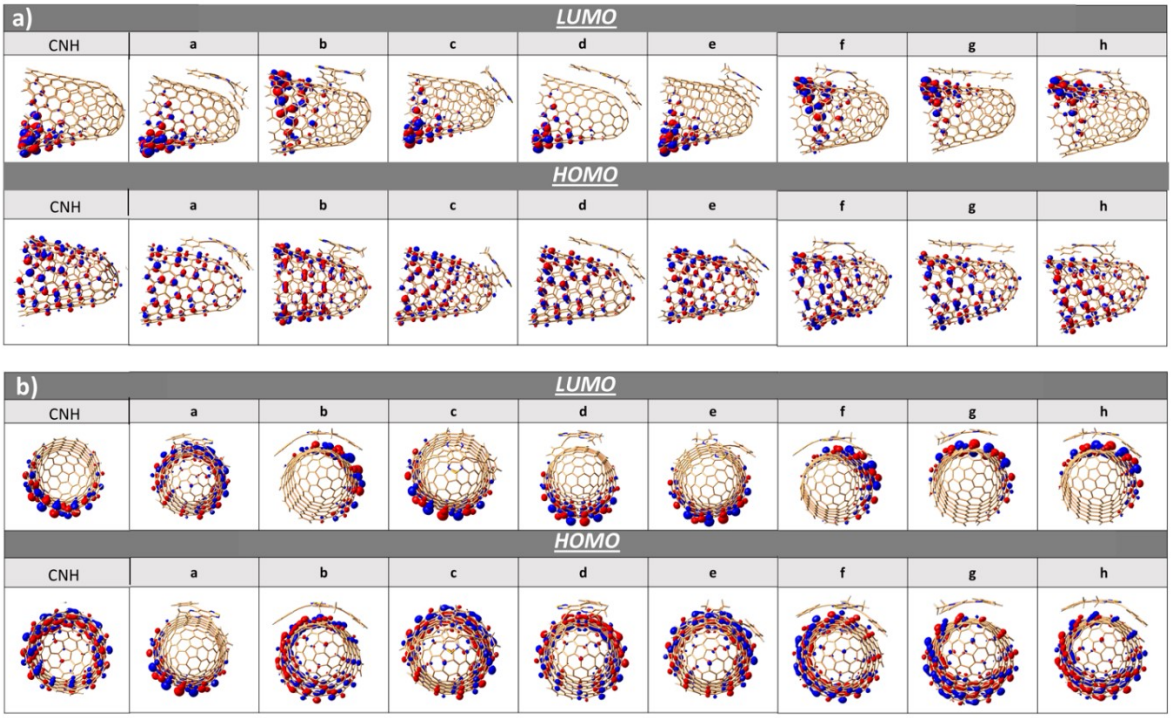

Figure S21 HOMO and LUMO orbitals for **CNH-2** in the different dispositions calculated at the ωB97XD /6-31G** level a)Front view, b) Top view.

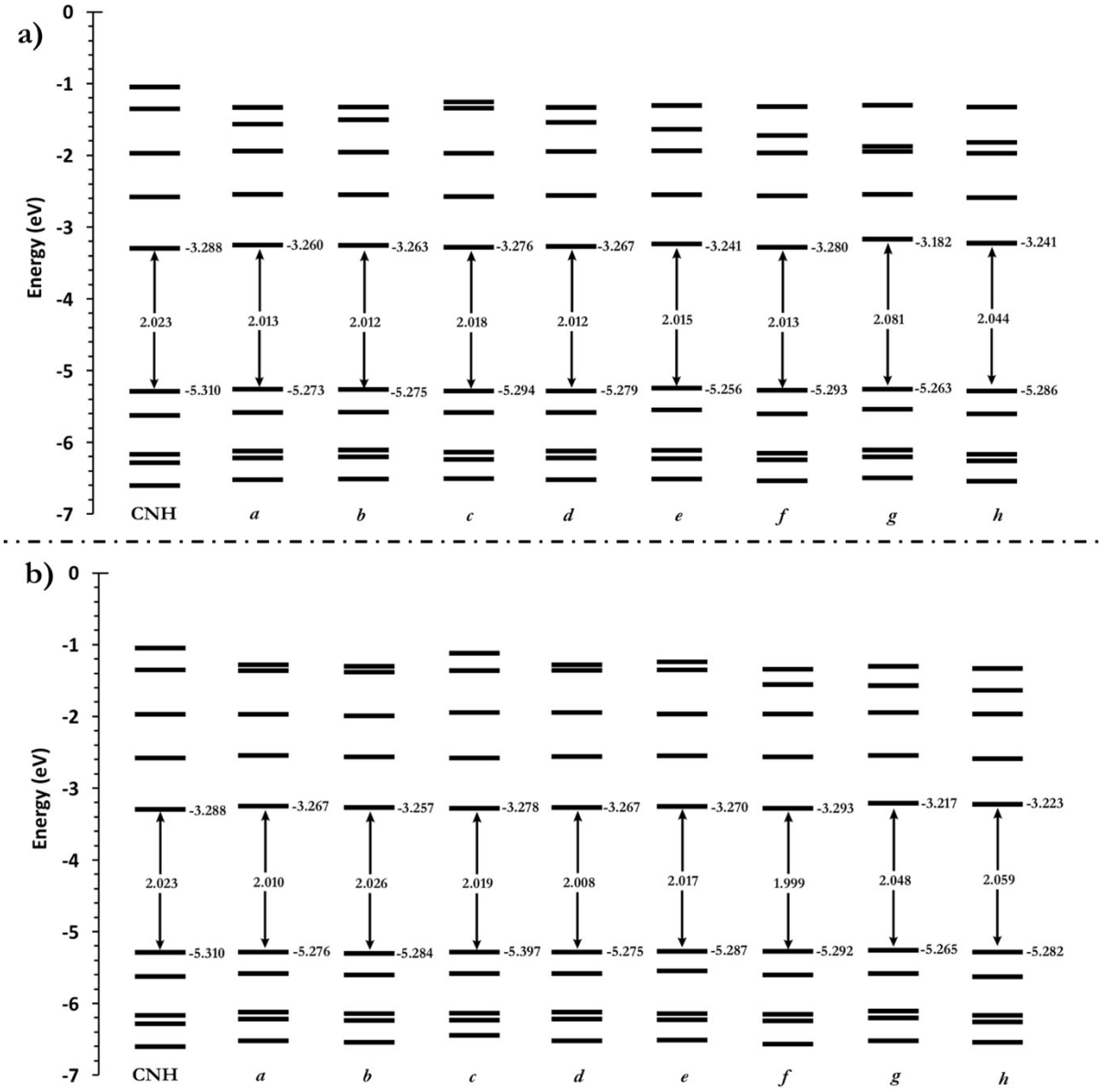

Figure S22 DFT-calculated molecular orbital energies for the different dispositions of a) **CNH-1** and b) **CNH-2**, compared to those calculated for unsubstituted CNH at the ωB97XD /6-31G** level.

Table S4. Mülliken charges (*e*) of **CNH-1** and **CNH-2** on the respective CNH and TDQ domains of the hybrids, computed at ωB97XD/6-31G(d,p).

Disposition	CNH-1		CNH-2	
	TDQ-1	CNH	TDQ-2	CNH
a	-0.0001	0.0001	0.0051	-0.0051
b	0.002	-0.002	-0.0111	0.0111
c	-0.0007	0.0007	-0.0070	0.0070
d	-0.0007	0.0007	-0.0054	0.0054
e	0.0042	-0.0042	-0.0101	0.0101
f	-0.0028	0.0028	-0.0192	0.0192
g	0.0092	-0.0092	-0.0034	0.0034
h	-0.0002	0.0002	-0.0101	0.0101

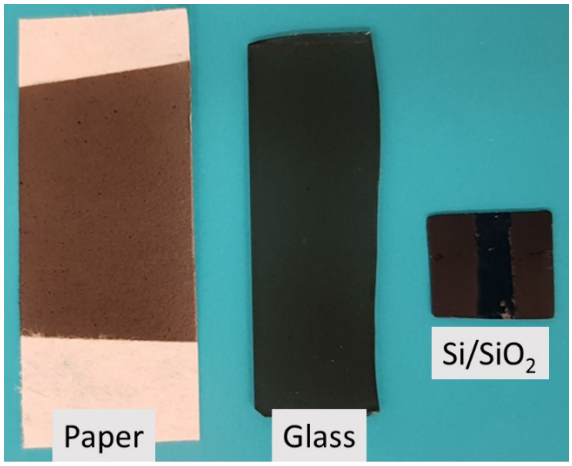

Figure S23. Optical photograph of sprayed-coated films deposited on the different substrates. The naked stripe on the Si/SiO_2 substrate (right) was created using a mask. This shows the possibility to create multiple configurations depending on the requirements of the application.

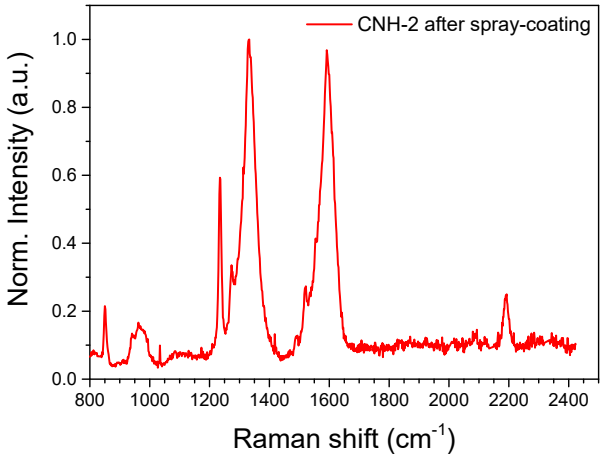

Figure S24. Raman spectrum of **CNH-2** after spray-coating on Si/SiO_2 showing that the SERS effect is preserved after the deposition process.

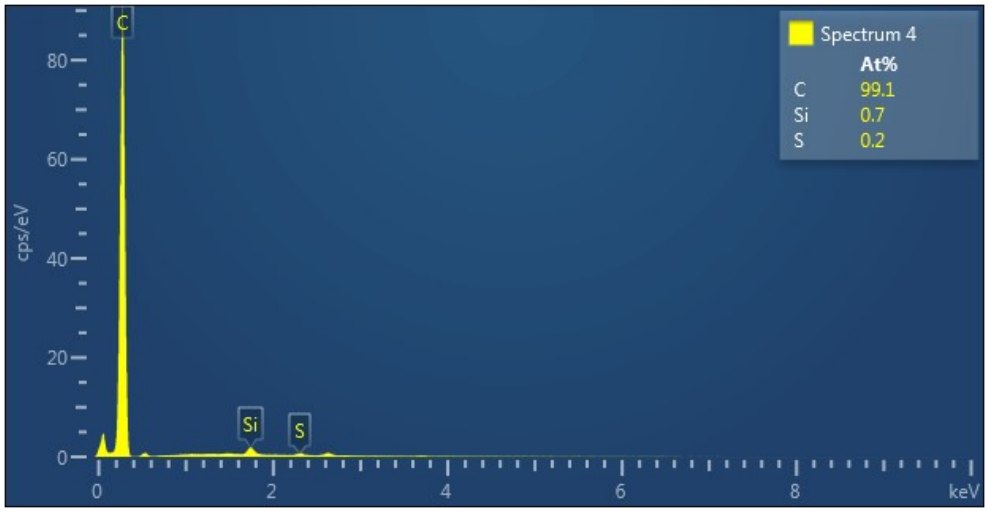

Figure S25. SEM-EDX analysis of **CNH-2** . The small amount of Si observed in the sample is attributed to the substrate.

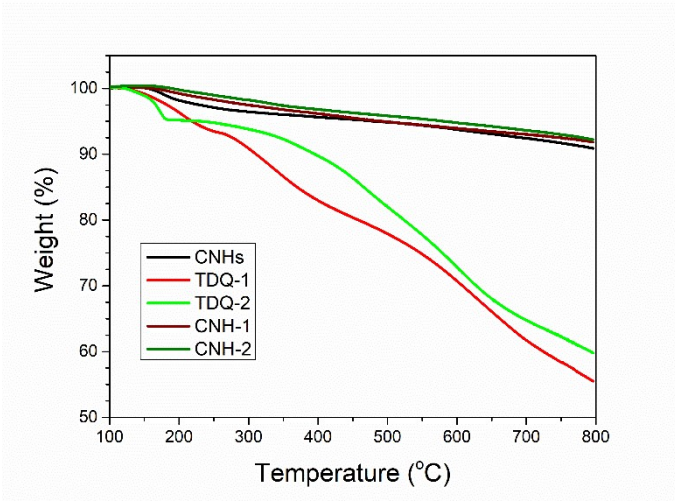

Figure S26. Thermogravimetric analyses of CNHs, the organic dyes and the hybrids.

4. References

1 J. Da Chai and M. Head-Gordon, *Phys. Chem. Chem. Phys.*, 2008, **10**, 6615–6620.

2 D. J. F. M. J. Frisch, G. W. Trucks, H. B. Schlegel, G. E. Scuseria, M. A. Robb, J. R. Cheeseman, G. Scalmani, V. Barone, G. A. Petersson, H. Nakatsuji, X. Li, M. Caricato, A. V. Marenich, J. Bloino, B. G. Janesko, R. Gomperts, B. Mennucci, H. P. Hratchian, J. V., 2016.

3 W. J. Hehre, K. Ditchfield and J. A. Pople, *J. Chem. Phys.*, 1972, **56**, 2257–2261.

4 M. M. Francl, W. J. Pietro, W. J. Hehre, J. S. Binkley, M. S. Gordon, D. J. DeFrees and J. A. Pople, *J. Chem. Phys.*, 1982, **77**, 3654–3665.

5 Y. Sugita, A. Kitao and Y. Okamoto, *J. Chem. Phys.*, 2000, **113**, 6042–6051.

6 E. Runge and E. K. U. Gross, *Phys. Rev. A*, 1984, **34**, 529–532.